# Three-dimensional numerical investigations of the morphology of type Ia SNRs

Donald C. Warren[1], John M. Blondin[1]

[1]*Physics Department, North Carolina State University, Raleigh, NC 27695-8202, USA*

Released 2012 Xxxxx XX

**ABSTRACT**

We explore the morphology of Type Ia supernova remnants (SNRs) using three-dimensional hydrodynamics modeling and an exponential density profile. Our model distinguishes ejecta from the interstellar medium (ISM), and tracks the ionization age of shocked ejecta, both of which allow for additional analysis of the simulated remnants. We also include the adiabatic index $\gamma$ as a free parameter, which affects the compressibility of the fluid and emulates the efficiency of cosmic ray acceleration by shock fronts. In addition to generating 3-D images of the simulations, we compute line-of-sight projections through the remnants for comparison against observations of Tycho's SNR and SN 1006. We find that several features observed in these two remnants, such as the separation between the fluid discontinuities and the presence of ejecta knots ahead of the forward shock, can be generated by smooth ejecta without any initial clumpiness. Our results are consistent with SN 1006 being dynamically younger than Tycho's SNR, and more efficiently accelerating cosmic rays at its forward shock. We conclude that clumpiness is not a necessary condition to reproduce many observed features of Type Ia supernova remnants, particularly the radial profiles and the fleecy emission from ejecta at the central region of both remnants.

**Key words:** Hydrodynamics – instabilities – ISM: supernova remnants.

## 1 INTRODUCTION

SN 1572, visible to the unaided eye on Earth, is now linked to the name of its most accurate observer, Tycho Brahe. Its remnant was rediscovered in radio frequencies almost four centuries later (Hanbury-Brown & Hazard 1952; Baldwin & Edge 1957), and has since been observed throughout the electromagnetic spectrum. SN 1006 was probably significantly brighter than SN 1572 to observers (Krause et al. 2008; Winkler, Gupta & Long 2003) around the globe when it first appeared, but its remnant was not identified until Gardner & Milne (1965). Both supernova remnants (hereafter SNRs) are resolvable to several hundred pixels across their diameters with the *Chandra* X-ray Observatory, and confirmation that the original supernovae were of type Ia (Baade 1945; Krause et al. 2008; Wu et al. 1983) make them ideal laboratories to test theories of supernova and remnant evolution.

Detailed observations have shown both Tycho's SNR and SN 1006 to be rich in structure. Of the numerous features observed in Tycho (Seward, Gorenstein & Tucker 1983; Dickel, van Breugel & Strom 1991; Reynoso et al. 1997; Warren et al. 2005) and SN 1006 (see Cassam-Chenaï et al. (2008) and references therein), three aspects of the remnants' morphology are relevant to this paper. One is

the nature of the clumpy, "fleecy" thermal emission located throughout Tycho and SN 1006, long since identified as ejecta in Tycho's case (Hamilton, Sarazin & Szymkowiak 1986) and that could be caused by the Rayleigh-Taylor instability. Another is the limb brightening effect, which can be used to identify the reverse shock but which is less pronounced than expected, or even absent, in many places around Tycho and SN 1006. The third is the radial structure of the remnants; that is, identifying the radial locations of the forward shock, contact discontinuity, and reverse shock and their projected positions.

It has long been argued that SNRs would be subject to fluid instabilities such as the Rayleigh-Taylor (Gull 1973) and the Kelvin-Helmholtz shear instability (Fryxell et al. 1991; Chevalier et al. 1992). Swept-up interstellar material (ISM) decelerates the denser ejecta behind the contact discontinuity, and fluctuations within the ejecta or ISM seed the Rayleigh-Taylor instability. Early treatment of this problem was either analytical or limited to one-dimensional numerical simulations looking for Rayleigh-Taylor-unstable zones in a radial profile (Gull 1973; Dickel et al. 1989). Nonlinearity and asymmetry limit the effectiveness of either approach, but advances in computing have since allowed SNRs and relevant instabilities to be modeled in multiple dimensions (Hachisu et al. 1990; Fryxell et al. 1991; Chevalier et

al. 1992). These results were expanded upon by other authors for a variety of other scenarios, such as ejecta clumping (Orlando et al. 2012), overdense ejecta "bullets" (Wang & Chevalier 2001), underdense ejecta "bubbles" (Blondin, Borkowski & Reynolds 2001), efficient particle acceleration at the shock fronts (Blondin & Ellison 2001; Ferrand et al. 2010), SNR interactions with a moving ISM (Velázquez et al. 2006), or asymmetries in the progenitor star and its environment (Blondin, Lundqvist & Chevalier 1996; Vigh et al. 2011).

SNRs expand and interact in three dimensions, but are observed in only two. Thus any comparison against observations must include some projection of the data, leading to projection effects such as limb brightening or overemphasis of irregular surfaces. Ferrand et al. (2010) present a three-dimensional simulation of one octant of a remnant, including line-of-sight projections of radiating material. Images both with and without emission from shocked ISM can be found in that paper, and show developed ejecta structures similar to those in Tycho. They do not, however, accurately capture the weak limb brightening effect observed by Warren et al. (2005); additionally, they find the reverse shock closer to the forward shock than observations suggest is the case for Tycho. The work of Orlando et al. (2012), performed over $4\pi$ steradians, uses volume renderings of the evolved remnants to match the radial structure of SN 1006. Inclusion of ejecta clumps alters the corrugation of the reverse shock, with the amount of disruption increasing as the size of the clumps increases. It also allows Rayleigh-Taylor structures generated by these clumps to reach and perturb the forward shock.

The primary question addressed by this paper is whether fluid instabilities alone are sufficient to explain the morphology of Tycho's SNR and SN 1006 as observed by *Chandra*. All three features of interest in these SNRs – the proximity of the contact discontinuity to the forward shock in projection, the fleecy nature of the central emission, and the indistinct limb brightening in some locations – would be affected by fluid instabilities at the contact discontinuity. Projection of a three-dimensional shell structure to a two-dimensional surface overemphasizes deviations from spherical symmetry, such as Rayleigh-Taylor fingers; this leads to errors in estimating the locations of the contact discontinuity and reverse shock. In particular, it has recently been proposed (Orlando et al. 2012) that clumpy ejecta is necessary to explain these features. We present in this paper complete three-dimensional simulations of a type Ia supernova remnant, covering the full angular range to allow unrestricted growth of Rayleigh-Taylor instabilities in all directions, without preferential treatment of certain wavenumbers.

In §2 of this article, we explain the model used in the simulations. In §3 we describe the initial conditions of the simulations and present results from the runs. In §4 the three-dimensional simulations are projected into a plane and compared against observations of Tycho's SNR and SN 1006. We discuss features of the projections in §5, in particular our estimation of the dynamical age of the two remnants. We conclude in §6.

## 2   THE EJECTA PROFILE

Dwarkadas & Chevalier (1998) compared several models for the ejecta profile of a type Ia supernova – constant, power law, and a new exponential profile for ejecta density – against several hydrodynamical models for type Ia explosion mechanisms and early spectral evolution. They found that the exponential density profile fit the models under consideration to a higher degree of accuracy than did the constant or power law profiles. In particular, the authors noted a good fit with the successful W7 model of Nomoto, Thielemann & Yokoi (1984) – see Figure 1 of Dwarkadas & Chevalier (1998) – and found that the profile began steep but flattened out over time. We adopt the exponential model developed in that paper, which uses a spherically symmetric density profile

$$\rho_{\rm SN} = At^{-3}e^{-v/v_e}. \tag{1}$$

Assuming that $r = vt$ at $t = t_0$, the constants $A$ and $v_e$ are found to be

$$A = \frac{6^{3/2}}{8\pi}\frac{M_e^{5/2}}{E^{3/2}} = 7.67 \times 10^6 \left(\frac{M_e}{M_{\rm Ch}}\right)^{5/2} E_{51}^{-3/2}\,{\rm g\,s^3\,cm^{-3}} \tag{2}$$

$$v_e = \left(\frac{E}{6M_e}\right)^{1/2} = 2.44 \times 10^8 \left(\frac{M_e}{M_{\rm Ch}}\right)^{-1/2} E_{51}^{1/2}\,{\rm cm\,s^{-1}}, \tag{3}$$

where $M_{\rm Ch} \approx 1.4\,M_\odot$ and $E_{51}$ are, respectively, the Chandrasekhar mass and the supernova energy in units of $10^{51}$ ergs.

We use the same scaling as Dwarkadas & Chevalier (1998):

$$R' = \left(\frac{M_e}{4/3\pi\rho_{\rm am}}\right)^{1/3} \approx 2.19 \left(\frac{M_e}{M_{\rm Ch}}\right)^{1/3} n_0^{-1/3}\,{\rm pc}, \tag{4}$$

$$V' = \left(\frac{2E}{M_e}\right)^{1/2} \approx 8.45 \times 10^3 \left(\frac{E_{51}}{M_e/M_{\rm Ch}}\right)^{1/2}\,{\rm km\,s^{-1}}, \tag{5}$$

and

$$T' = \frac{R'}{V'} \approx 248 \left(\frac{M_e}{M_{\rm Ch}}\right)^{5/6} E_{51}^{-1/2} n_0^{-1/3}\,{\rm yr}, \tag{6}$$

with $n_0 = \rho_{\rm am}/(2.34 \times 10^{-24}\,{\rm g})$ being the number density of the interstellar medium, assuming a 10:1 H:He ratio. Pressure values were scaled to the ram pressure $\rho_{\rm am}V'^2$. This scaling is not unique; McKee & Truelove (1995) adopt a different scaling in their treatment of SNRs. For this paper we adopt the convention that primed lowercase letters denote the real, physical quantities, while unprimed lowercase letters are used for their scaled counterparts, e.g. $t = t'/T'$.

Though Dwarkadas & Chevalier (1998) considered multiple different ejecta profiles in their one-dimensional study, we use only their exponential profile here. Other work (Ferrand et al. 2010) has been performed in 3-D using the power law profile, against which the results presented in this paper can be compared. To our knowledge, no multi-dimensional simulations have used the constant profile.

## 3 THE NUMERICAL MODEL

To run the simulations we used the hydrodynamics code VH-1, which solves the Euler equations for fluid flow using the piecewise parabolic method with a Lagrangian remap step – see Colella & Woodward (1984) for a thorough description of the procedure. The base hydrodynamics code was extended with a subroutine to calculate ionization age of ejecta elements, which could then be used to generate emission maps for comparison against observations.

In order to save computing time, simulations were initiated in one dimension, then continued in 3-D at a later time. The starting time used in one dimension was one day, or $t = 2.74 \times 10^{-3}$ yr$/T' = 1.1 \times 10^{-5} (M_e/M_{\mathrm{Ch}})^{-5/6} E_{51}^{1/2} n_0^{1/3}$. The grid at initialization started at $r_{\min} = 5 \times 10^{-5}$ with $r_{\max}/r_{\min} = 2.4$, so that the forward edge of the grid was just beyond where the exponential profile reaches a density equal to the ISM. The grid contained 480 zones, for a resolution of $\Delta r/r_{\max} \approx 1.2 \times 10^{-3}$; this was deemed to be an acceptable balance between resolution and computing time for the three-dimensional runs (a brief discussion of resolution effects occurs in the next paragraph, but all 3-D runs were performed at this resolution). The initial conditions within the ejecta were a radial velocity of $v = r/t$, density set according to the exponential profile, pressure calculated as an ideal gas at a temperature of 5 K, and angular velocities set to 0. The ISM was assumed to be at rest, with a density of unity, and cold. The interior radial boundary condition was set to the exponential model with no angular velocity, and the exterior radial boundary matched the ISM described previously. To follow the motion of the shocks over many doubling times, the grid tracked the forward shock, advancing and expanding by a small amount whenever the forward shock moved within six zones of the outer edge of the grid.

Early two-dimensional runs with an effective adiabatic index of $\gamma = 5/3$ showed that resolution had a minimal effect on the gross structure of the instabilities generated. At $t = 2.0$ in simulations with resolutions between $\Delta r/r_{\max} \approx 4.9 \times 10^{-4}$ and $\Delta r/r_{\max} \approx 2.4 \times 10^{-3}$, the dominant wave mode was consistent across all resolutions, though at higher resolutions more fine structure was present. Changing the resolution has two effects beyond modifying the power spectrum of Rayleigh-Taylor instabilities. First, increasing the resolution would allow for enhanced Kelvin-Helmholtz instability formation, which should in turn accelerate the onset of the instability saturation period discussed in the next paragraph. Second, as the effective adiabatic index decreases, a high resolution becomes necessary to resolve the small-scale structure associated with highly compressible fluid.

One constant through all of the two-dimensional runs was the presence of three "epochs" regarding instabilities. In the first of these, the initial seeds (random perturbations of either density, radial velocity, or pressure; or a long-wavelength perturbation of radial velocity) generated Rayleigh-Taylor fingers with a wavelength of a few grid zones, which then cascaded into larger structures. The second epoch was a period of instability saturation: multiple cycles in which Rayleigh-Taylor fingers appeared, grew toward the forward shock, experienced shear from the Kelvin-Helmholtz instability along their edges, and fell back towards the reverse shock. An instability "freeze out" divided the second and third epochs. After the freeze out, it became possible to track individual RT structures to the end of the simulation, since production of new RT structures slowed down and a second cascade to larger structures occurred. The instability saturation period has been reported for both the power law (Chevalier et al. 1992; Kane, Drake & Remington 1999; Blondin & Ellison 2001) and exponential (Dwarkadas 2000; Wang & Chevalier 2001) models. Because of this epoch, we expect that any trace of the initial perturbation, at least for the small magnitudes applied in our simulations, is washed away before the fingers freeze out.

We further investigated the saturation period by changing the times at which 1-D runs were expanded to two dimensions and further evolved. One-dimensional runs were carried out to $t = 3.65 \times 10^{-5}$ (the earliest time at which the contact discontinuity appeared as a minimum in the density profile rather than as a kink), $t = 3.65 \times 10^{-4}$ and $t = 3.65 \times 10^{-3}$ before mapping to two dimensions and seeding instabilities. The 2-D run begun at $t = 3.65 \times 10^{-4}$ achieved the saturation exhibited by the earliest start time. The $t = 3.65 \times 10^{-3}$ run never reached the instability saturation epoch; the first generation of RT fingers were still identifiable at the end of the simulation, at $t = 2.0$. As long as the mapping from one to multiple dimensions occurred early enough, the simulations achieved saturation and were largely indistinguishable. We therefore saved computation time in the three-dimensional runs by starting them at $t = 3.65 \times 10^{-4}$ without any apparent changes to the evolution of the remnant. The importance of the instability saturation period to our results bears restating: covering four or more decades of time allowed the instabilities to saturate and wash out traces of the initial perturbations, while simulating three decades resulted in clear imprints of the initial perturbations in the final state of the ejecta. Orlando et al. (2012) used only two decades of expansion time in their simulations, from an age of 10 years to an age of 1000 years, and their runs with smooth ejecta are still clearly dominated by grid effects at late times (note the quadrilateral symmetry in figure 6 of that paper, a product of the Cartesian grid used in the simulations).

Given the long-standing evidence in the literature that efficient cosmic-ray acceleration at shock fronts can dramatically effect the eventual morphology of an SNR, three different three-dimensional runs were performed. As an approximation for energy loss at shock fronts, we used the procedure of Blondin & Ellison (2001), globally adjusting the adiabatic index of the fluid to increase its compressibility. The run with an adiabatic index $\gamma = 5/3$ (ideal gas with a strong shock compression ratio $\sigma = 4$) served as a control. To compare against this we performed simulations with $\gamma = 4/3$ ($\sigma = 7$) and $\gamma = 6/5$ ($\sigma = 11$).

The three-dimensional runs covered the full $4\pi$ steradians, allowing instabilities everywhere in the simulation to grow without boundary effects, and preventing grid-induced preferred wavenumbers. To avoid geometrical singularities at the poles and allow for a more uniform $\Delta\theta$ and $\Delta\phi$ across the grid, we employed specialized Yin-Yang grid of two congruent parts with angular extent $\pi/2$ in $\theta$ and $3\pi/2$ in $\phi$ (Kageyama & Sato 2004). A one-dimensional kickstarting run was taken out to a scaled time of $t = 3.65 \times 10^{-4}$, then swept across the grid to form the basic three-dimensional profile, discarding the innermost quarter of the 1-D grid –

zones well inside the reverse shock even at the end of the simulation. The 3-D runs used a grid resolution of $\Delta r/r_{max} \approx 1.2 \times 10^{-3}$, in keeping with the 1-D kickstart runs. Though "cubic" zones with $\Delta r \approx r\Delta\theta \approx r\sin\theta\Delta\phi$ would have been preferred, memory and computation time constraints required the angular resolution be decreased by a factor of roughly two from the cubic value. The resolution of the three-dimensional runs was ultimately $360 \times 360 \times 1080 \times 2$ ($r \times \theta \times \phi$, with the final factor of 2 representing the Yin and Yang sections of the grid), with $r_{max}/r_{min} = 1.78$. We deemed resolutions lower than this to be insufficient to capture the structures expected in the runs with lower adiabatic indices.

The instability seed for our simulations was a random multiplier between 0.95 and 1.05 applied independently to the density of each cell containing shocked ejecta; two-dimensional runs showed that the form of any initial perturbation has a negligible effect on the final shape of the simulation remnant as long as the simulation is evolved long enough to include the instability saturation period discussed in the previous paragraph.

Finally, ionization age of shocked ejecta was tracked to investigate its effect on observed morphology. As used in our simulations, the ionization time is a computationally inexpensive parameter that can then be used to provide a more accurate emission map than a basic density-squared model can. We first assumed that the electron density $n_e$ is proportional to the fluid density throughout the remnant. During each cycle we calculated the temperature of every ejecta element; elements hotter than our cutoff temperature of $5 \times 10^5$ K were assumed to have been shocked, and we updated the ionization time in each such cell by $\tau_{new} = \tau_{old} + \rho \cdot dt$. Over the duration of our simulations, shocked ejecta never dropped below the cutoff temperature, so we could track shocked ejecta solely by temperature. We further assumed that iron is the sole contributor of free electrons to the ejecta; this is a very rough approximation, and future work might include additional species of ions for a more accurate picture. Using neon-like iron (16 free electrons per nucleus), the scale factor for ionization age is

$$\tau_{scale} = \frac{\rho_{am} \cdot N_A \cdot 16}{55.8} \cdot T'$$
$$\approx 3.15 \times 10^9\, n_0^{2/3} E_{51}^{-1/2} \left(\frac{M_e}{M_{Ch}}\right)^{5/6} \text{cm}^{-3}\text{s.} \quad (7)$$

where $N_A$ is Avogadro's number and 55.8 the molecular mass of iron.

## 3.1   Dependence on time

As mentioned in section 2, the only parameter affecting the morphology of a particular run is the scaled time. One of the primary questions addressed in this paper is whether the fleecy ejecta structures observed in type Ia SNRs are consistent with homogeneous ejecta. If the structures are solely due to hydrodynamic instabilities, their size and distribution could indicate the age of the remnant, providing a constraint on the three key parameters of the exponential model ($M_{ej}$, $n_0$, and $E_{51}$). For all three runs ($\gamma = 5/3$, $\gamma = 4/3$, and $\gamma = 6/5$) we tracked the simulations longitudinally in time. Figure 1 shows the $\gamma = 5/3$ run at three different times. Isosurfaces have been drawn of the three key interfaces – the

**Table 1.** Interface Radii and Ratios from 3-D Data for $\gamma = 5/3$

| $t$ | $R_{RS}$ | $R_{CD}$ | $R_{FS}$ | $R_{RS} : R_{FS}$ | $R_{CD} : R_{FS}$ |
|------|------|------|------|------|------|
| 0.12 | 0.249 | 0.265 | 0.297 | 0.838 | 0.892 |
| 0.75 | 0.716 | 0.800 | 0.952 | 0.752 | 0.840 |
| 2.0 | 1.005 | 1.229 | 1.615 | 0.622 | 0.761 |

Here and throughout the paper, $R_{CD}$ is used to represent $< R_{CD} >$, the radius averaged over all $4\pi$ steradians.
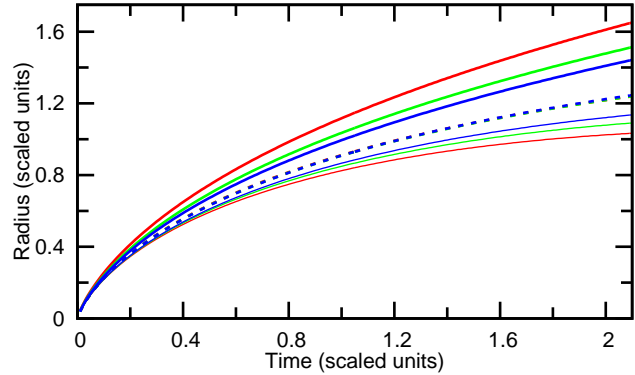
**Figure 2.** Interface locations as a function of time and adiabatic index for the exponential model in one dimension. The forward shock is tracked by thick solid lines, the reverse shock by thin solid lines, and the contact discontinuity by dashed lines. The curves for $\gamma = 5/3$, $\gamma = 4/3$, and $\gamma = 6/5$ are in red, green, and blue respectively. The three curves for the contact discontinuity are separated by less than the width of the line used to show them.

reverse shock, the contact discontinuity (where the ejecta fraction of fluid elements is 0.5), and the forward shock. All images in figure 1 are scaled to the same angular size, but the data presented in table 1 provide the relative scale. All images occur after the instabilities freeze out, so the production of new RT structures is negligible compared to the merging of existing structures. The three images have several distinguishing features, such as the proximity of the various fluid discontinuities and the structure at the forward and reverse shocks.

The three interfaces consistently diverge from each other over the course of the simulation, illustrated by the one-dimensional simulations shown in figure 2: the contact discontinuity decelerates less than the reverse shock, and the forward shock decelerates less than either. Consequently, as time progresses there is less interaction between the two shock fronts and the Rayleigh-Taylor structures at the contact discontinuity. At the earliest time shown in figure 1, the interaction between the contact discontinuity and the reverse shock is clear, as the features on the reverse shock are similar in angular size and spacing to the Rayleigh-Taylor structures just outside them. As the reverse shock recedes from the contact discontinuity, the shock front smooths out, the number of features and their radial extent shrinks, and their angular size grows. A similar process can be seen occurring at the forward shock: by $t = 2.0$ the entire shock front has a radial dispersion of less than a single radial zone on the grid.

The images in figure 1 show that the Rayleigh-Taylor structures in shocked ejecta trend toward larger angular
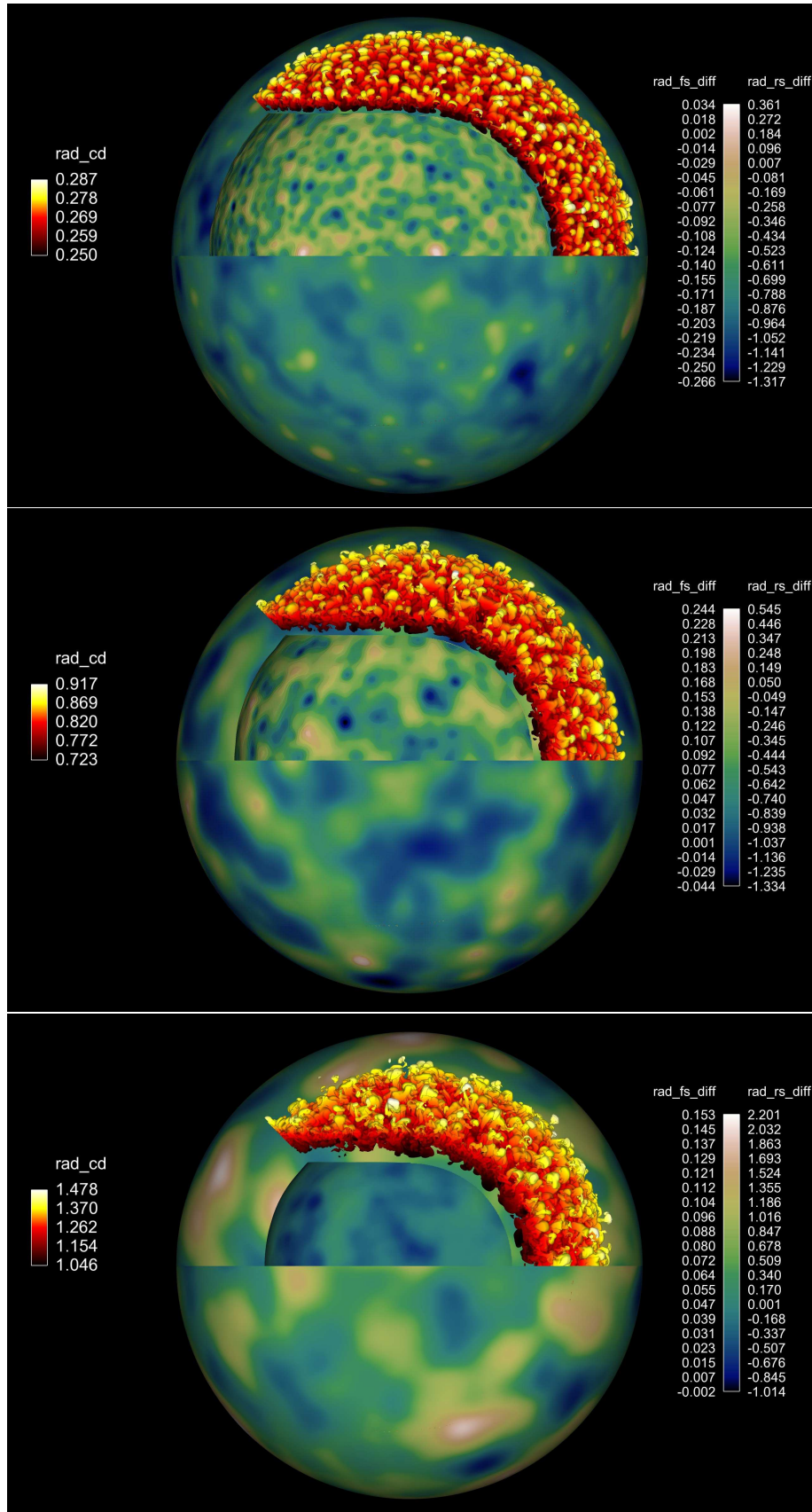
**Figure 1.** Isosurfaces for the reverse shock, contact discontinuity, and forward shock for the $\gamma = 5/3$ run at three times: $t = 0.12$, $t = 0.75$, $t = 2.0$. The color scale for the contact discontinuity is absolute radial position, while the color scale for the forward and reverse shocks is percent difference from the average value for that interface as given in table 1.
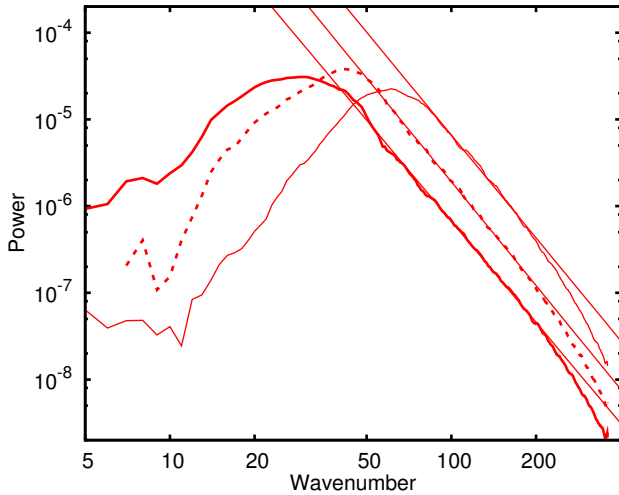
**Figure 3.** Power spectra for the radial ejecta column density in the $\gamma = 5/3$ simulation. The curves for early time ($t \approx 0.15$), middle time ($t \approx 0.75$) and late time ($t = 2.0$) are thin solid line, dashed line, and thick solid line respectively. The overlaid lines are best fits to power laws, $P \propto l^{-\alpha}$, with all exponents $\sim 3.9$. All spectra have been normalized and smoothed.

size at later times. To further test this, we integrated the total shocked ejecta density in radial columns over all $4\pi$ steradians. We then used the SHTOOLS package[1] to calculate power spectra for the generated image. The results are shown in figure 3, which plots the normalized power versus degree of spherical harmonic. The power spectrum's peak moves to lower values of $l$ as the simulation progresses, from $l \sim 60$ at the earliest time to $l \sim 30$ at $t = 2.0$. The spectra between the peak and $l \approx 200$ can be fit to a power law in each case, with an exponent around 3.9. Higher than $l \approx 200$ the bottleneck effect (Dobler et al. 2003) caused a steepening of the power spectra in every case shown. Though the slope of the power spectrum does not substantially change with time, it is clear that power is transfered from higher wavenumbers to lower wavenumbers over the course of the simulation.

All of the fits are significantly steeper than fitted power laws to the observed contact discontinuity of Tycho's SNR, $P \sim k^{-1.5}$ (Warren et al. 2005). Further, the difference is in the wrong direction: when the naturally two-dimensional surface of the CD is projected to a single line around the remnant, projection effects should act to smooth out some of the high-frequency power, steepening the power spectrum relative to that of the original 2-D surface. (See Appendix A for additional information.) While both power laws extend to a wavenumber of about 180, our peak occurs at a much higher wavenumber ($l \sim 30$) than theirs ($l \sim 6$).

## 3.2 Dependence on adiabatic index

Support abounds in the literature for the idea that efficient cosmic-ray acceleration impacts the evolution and morphology of SNRs. We find that increased shock compressibility leads to dramatic differences in the morphology of the
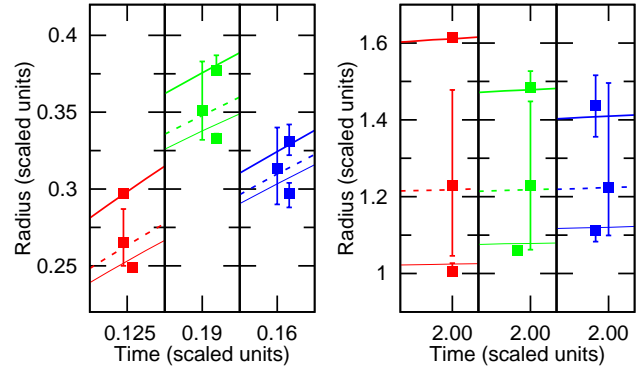
[1] Available at http://shtools.ipgp.fr/



**Figure 4.** Interface locations as a function of time and adiabatic index for the exponential model in one and three dimensions. Fluid discontinuities from 1-D runs are colored and marked as in figure 2. Interface locations in the 3-D runs are listed in tables elsewhere in the paper. The plots for $\gamma = 5/3$, $\gamma = 4/3$, and $\gamma = 6/5$ appear as the left, middle, and right panels in each triplet, respectively. *Left*: Close-ups of the 1-D interface locations around $t = 0.15$, with the 3-D interface locations plotted for comparison. The error bars show the maximum and minimum extent of the interface. To prevent overlap of 3-D error bars, some shocks are plotted slightly to the right of their proper position. *Right*: As before, but around $t = 2.0$; shifting here is to the left.

**Table 2.** Interface Radii and Ratios from 3-D Data for $t = 2.0$

| $\gamma$ | $R_{RS}$ | $R_{CD}$ | $R_{FS}$ | $R_{RS} : R_{FS}$ | $R_{CD} : R_{FS}$ |
|---|---|---|---|---|---|
| 5/3 | 1.005 | 1.229 | 1.615 | 0.622 | 0.761 |
| 4/3 | 1.060 | 1.228 | 1.484 | 0.714 | 0.827 |
| 6/5 | 1.112 | 1.224 | 1.438 | 0.773 | 0.851 |

shocked ejecta and of the two shock fronts. In this section we will describe the effect of the adiabatic index on four aspects of morphology: the shape and location of the contact discontinuity, the shape and location of the forward and reverse shock fronts, the power spectrum of the contact discontinuity, and the deceleration parameter.

Under the assumption of spherical symmetry, reducing $\gamma$ from 5/3 has the most immediate morphological effect of changing the shock locations of the remnant at any particular time, as illustrated in figure 2. This does not apply to the contact discontinuity: the difference between the three 1-D runs' contact discontinuities is less than the width of the line used to plot their position in figure 2. We explain this with an appeal to conservation of momentum. In the thin shell limit of Gull (1973), the entirety of the shocked ejecta and the swept-up ISM are contained at a single radius. As the gas becomes less compressible, both the ejecta piston and the shocked ISM regions expand in volume relative to the thin shell limit. This means that both shocked ejecta and the shocked ISM increase in mass, sweeping up additional matter that was beyond either shock front when the fluid was more compressible. The additional inertia of the shell of ISM is roughly balanced out by the gained momentum of the piston, and at a given time the radius of the contact discontinuity stays roughly constant as the compression ratio drops from $\sigma = \infty$ to $\sigma = 4$. This effect is not permanent: the thickness of the regions of shocked fluid in-
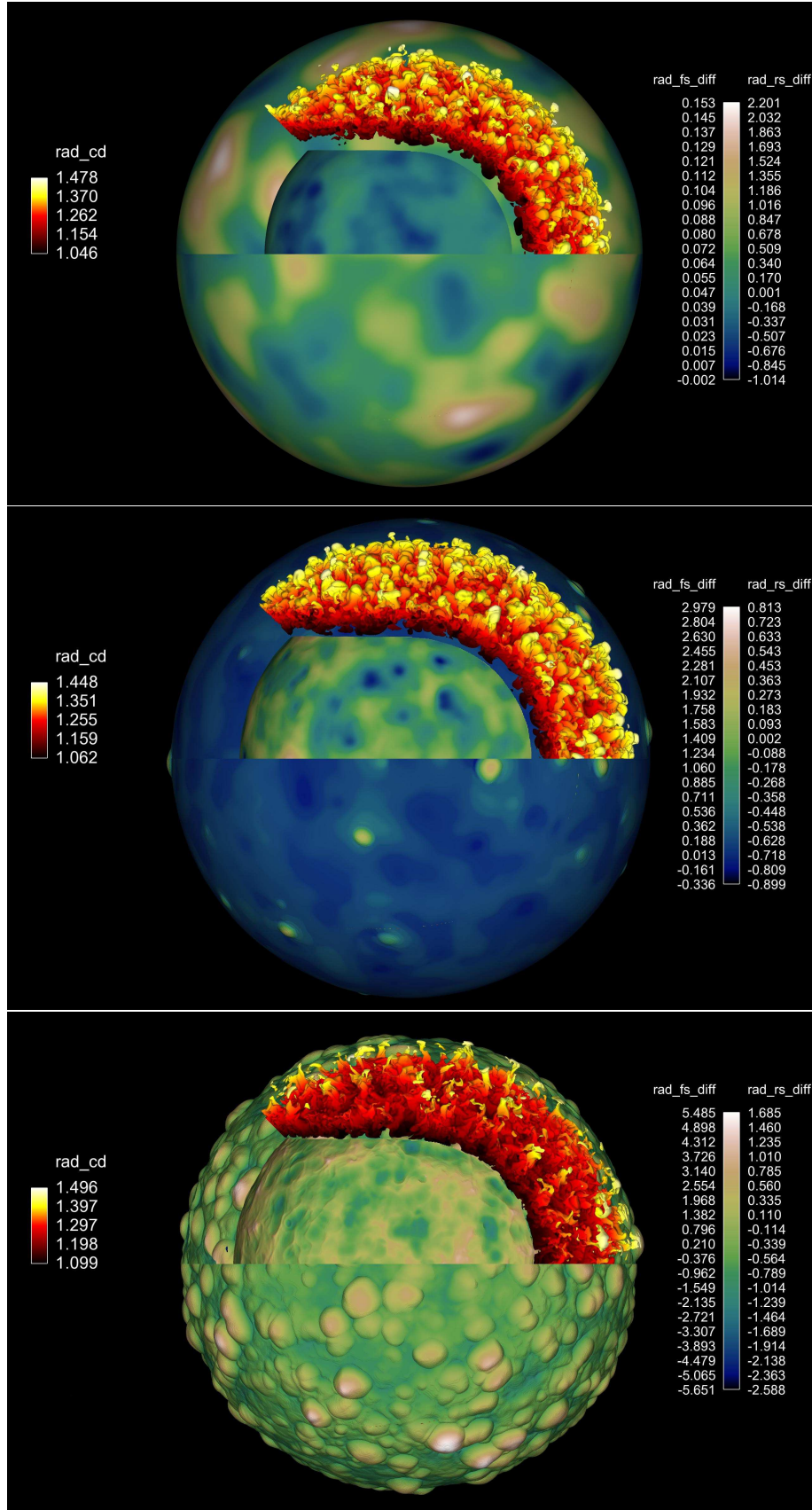
**Figure 5.** Isosurfaces for the reverse shock, contact discontinuity, and forward shock at $t = 2.0$ for all three runs. The color scale for the contact discontinuity is absolute radial position, while the color scale for the forward and reverse shocks is percent difference from the average value for that interface as given in table 2.

creases constantly and reduces the appropriateness of the thin-shell approximation. After a few times $t'$ (see section 2), runs with lower compressibilities start to decelerate relative to runs with greater compressibilities. The likely ages of Tycho's SNR and 1006 fall well short of the point of separation, however, so for the purposes of this work the location of the contact discontinuity is independent of compressibility.

Beyond spherical symmetry, the shape of the interfaces can also vary, in some cases substantially. Figure 5 shows all three three-dimensional runs at a scaled time of $t = 2.0$. As before, the remnants have been scaled to the same size, with the actual radii provided in table 2.

In all of the tables in this paper, we list the location of the contact discontinuity as a single number, its average location. In actuality the contact discontinuity has a very complex shape that depends on both the remnant's age and the compressibility of the fluid, as can be seen in figures 1 and 5. By $t = 2.0$, the CD is spread out over many radial zones (its radial extent is as high as 29% of its maximum radius for the images in figure 5), and at many places around the remnant occurs multiple times in a single radial column (e.g., locations with RT mushroom caps above the base of the structure). Using just the average location of the contact discontinuity is a great simplification. Reducing the structure of the CD to a single number is nonetheless justified: as in one dimension (see figure 2), table 2 shows that the average radius of the contact discontinuity in three dimensions is nearly constant across all three values of $\gamma$ at $t = 2.0$. Despite the independence of the CD's average radius and the compressibility of the gas, as $\gamma$ decreases there is a bias towards more ejecta close to the reverse shock; this is visible in figure 5 as a shift in color of the contact discontinuities away from yellow/white and toward red/black.

The average location of the forward and reverse shocks in each of the 3-D runs is slightly less consistent with their radial positions in the corresponding 1-D simulations, as noted in figure 4 (the forward and reverse shocks have been plotted slightly to the left or right when needed for the sake of clarity). Both shock fronts are slightly more advanced in three dimensions – the reverse shocks are at a lower average radius, and the forward shocks at a greater average radius. The advanced location of the forward shocks is likely due to interaction between the shock front and Rayleigh-Taylor fingers at the contact discontinuity. As the adiabatic index decreases and interaction between the two interfaces increases, protrusions appear at the forward shock that pull the average location ahead of where it would be in one dimension. Figure 4 also shows error bars marking the maximum and minimum radii for each interface, further demonstrating the interaction and bubbles already mentioned.

Figure 5 offers clear support for the effect of Rayleigh-Taylor fingers on the shape and location of the forward and reverse shocks. The $\gamma = 5/3$ run shows very smooth forward and reverse shocks – the forward shock is located in the same radial zone everywhere in the remnant, while the reverse shock is spread over just a few zones. There is a large gap between both shocks and the contact discontinuity, the likely reason for the smoothness of both shock fronts. Although a major assumption behind our simulations was smooth ejecta, the second and third images in figure 5 demonstrate that smooth ejecta alone is not sufficient to guarantee smooth forward and reverse shocks. The
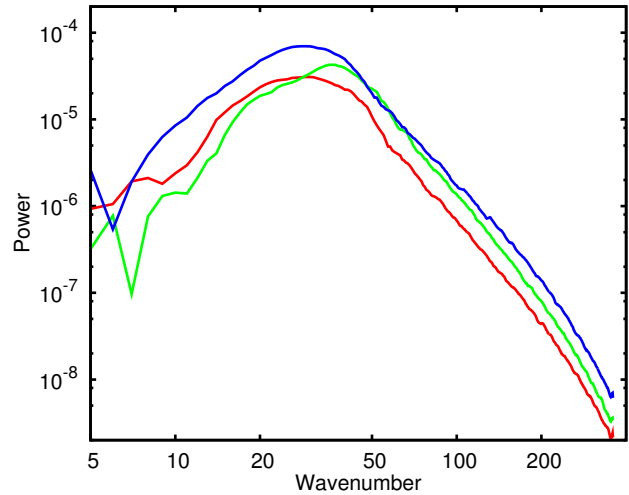


**Figure 6.** Normalized power spectra for the radial ejecta column density of the 3-D simulations at $t = 2.0$. The curves for $\gamma = 5/3$, $\gamma = 4/3$, and $\gamma = 6/5$ are in red, green, and blue respectively. The exponents to fitted power laws (not plotted here) are 3.9 for $\gamma = 5/3$, 4.0 for $\gamma = 4/3$, and 3.5 for $\gamma = 6/5$.

$\gamma = 4/3$ run shows definite evidence of interaction at the forward shock: the majority of the interface is as smooth as its $\gamma = 5/3$ counterpart, but a few tens of bumps can be seen where Rayleigh-Taylor fingers reached far enough outward to perturb the sphericity of the forward shock. The situation is repeated at the reverse shock, where features on the same angular scale as the RT structures are visible and the shock front itself has a radial extent of $\approx 0.02$ times its average radius in the data. When $\gamma = 6/5$, the increased compressibility of the fluid has a marked effect on the shape of the remnant. There is abundant evidence of interaction between the contact discontinuity and the forward and reverse shocks (at the right edge of the image a Rayleigh-Taylor finger can even be seen in the process of creating one of the numerous bubbles visible on the forward shock).

As the adiabatic index decreases from $5/3$ to 1, the ejecta become more compressible and Rayleigh-Taylor structures can be thinner. This results in more power at small wavelengths in the simulations with $\gamma < 5/3$, illustrated in figure 6, which was created in the same manner as figure 3. The figure shows an essentially monotonic increase in power at high wavenumbers as $\gamma$ decreases (the $\gamma = 4/3$ run's power spectrum peaks later, around $l = 40$, than do the power spectra of the other two runs, which peak around $l = 30$). Additionally, fitted power laws become shallower as the adiabatic index approaches 1, with the exponent dropping from 3.9 ($\gamma = 5/3$) to 3.5 ($\gamma = 6/5$).

The deceleration parameter ($m = vt/r$) of the forward shock, as shown in figure 7, is another point of comparison between the radial structure in 1-D and its averaged equivalent in 3-D. Calculation of $m$ in the 1-D case is simple, as one can easily track the motion of the forward shock, to grid-zone accuracy in space and arbitrary accuracy in time, and arrive at a value for the forward shock expansion velocity. For the 3-D runs, we used the Rankine-Hugoniot conditions for a strong shock to calculate the forward shock velocity in terms of the downstream pressure, upstream den-
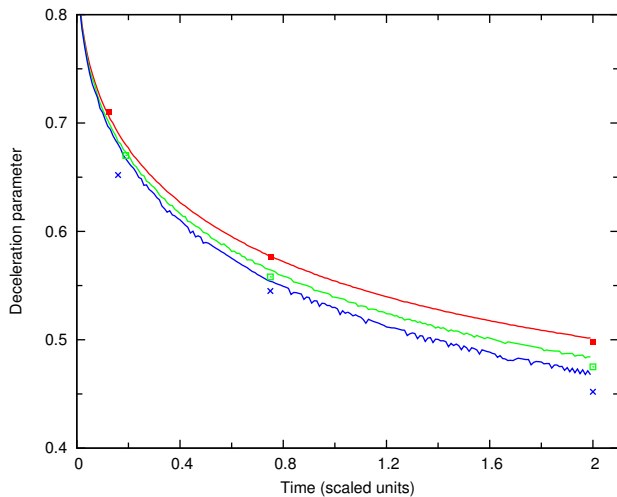
**Figure 7.** The deceleration parameter as a function of time and adiabatic index for the exponential model. The curves for one dimension and $\gamma = 5/3$, $\gamma = 4/3$, or $\gamma = 6/5$ are in red, green, or blue respectively. Overlaid are points showing the calculated deceleration parameter for the 3-D runs at selected times.

sity, and adiabatic index. The various deceleration parameters are collected in figure 7. As in figure 4, the deceleration parameter in one dimension for each value of $\gamma$ is shown as a curve, with the corresponding 3-D values overlaid as points. At any particular time decreasing the adiabatic index reduces the deceleration parameter, and a lowered adiabatic index reduces the time at which the remnant reaches a particular value of the deceleration parameter. The curves and points of figure 7 are in close agreement everywhere, with the exception of the $\gamma = 6/5$ run. There, the bubbles at the forward shock lead to a substantial solid angle where the shock normal isn't radial. This induced angle appears as a smaller radial expansion speed $v$, and so a smaller deceleration parameter. Restricting the averaging process to only those grid zones on the forward shock whose normal is within $15°$ of the radial direction eliminates most of the bubbles but retains the largely spherical base visible in figure 5. It also moves the calculated 3-D deceleration parameters to within a few percent of the 1-D values, in line with the other values for $\gamma$; the corrected values are shown in figure 7, rather than the uncorrected numbers.

## 4 OBSERVATIONAL IMPLICATIONS

To facilitate comparison with the X-ray observations of Tycho and SN 1006, we now present line-of-sight projections from the three-dimensional data sets. We assume thermal emission from shocked ejecta to be proportional to the square of gas density. To mimic the effects of emission turn-on as shocked ejecta are ionized, a cutoff in ionization age is implemented by which emission from some ejecta elements can be excluded (see section 4.3). Synchrotron emission from the forward shock is visualized assuming that both relativistic electron energy density $u_e$ and magnetic field energy density $u_B$ are proportional to the pressure (i.e. nonlinear amplification of the magnetic field). Then, since synchrotron volume emissivity $j_\nu$ is proportional to $u_e B^{(s+1)/2}$, with $s$
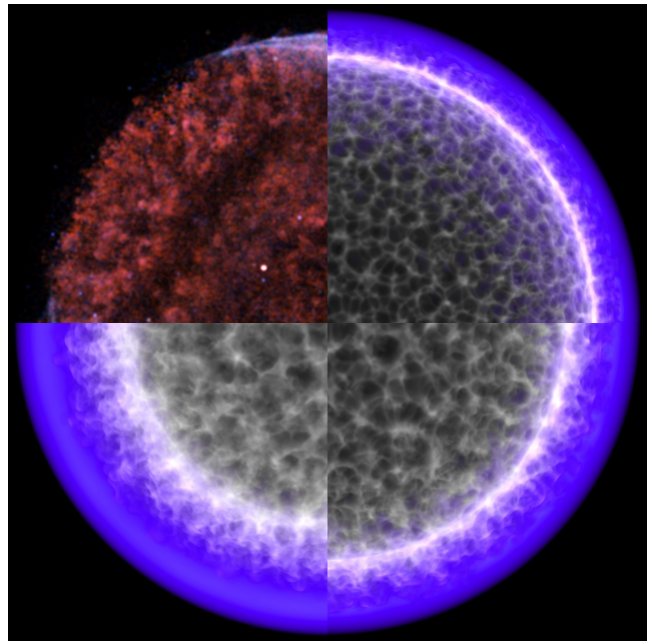


**Figure 8.** Images showing the effect that dynamical age has on the morphology of the remnant. The SE quadrant of SN 1006 is included at the top left for comparison. All three remaining images come from the $\gamma = 5/3$ run. Clockwise from the top right: $t = 0.12$, $t = 0.75$, $t = 2.0$. Image of SN 1006 taken from Cassam-Chenaï et al. (2008).

being the electron energy index (i.e. $N(E) \propto E^{-s}$) (Pacholczyk 1970), we have $j_\nu \propto P^{(s+5)/4}$. As $s \cong 2.2$ for both SN 1006 and Tycho (Green 2009), the synchrotron emissivity is calculated as $P^{1.8}$. X-ray synchrotron emission decays more rapidly away from the forward shock than radio emission, so our crude model results in a more diffuse shell of emission around the ejecta than would be present with a more refined treatment. In all images of projections in this section (with the exception of figure 10), ejecta emission is in white and synchrotron emission is in purple.

Using these images, we take a more in-depth look at the distribution and character of emission from shocked ejecta, the shape and location of the projected contact discontinuity, and the strength of the limb brightening effect under ionization age cutoffs to emission.

### 4.1 Fleece

Figure 8 compares the SE quadrant of SN 1006 against projected quadrants from the $\gamma = 5/3$ run at the same three times shown (in 3-D) in figure 1. Immediately apparent is that the emission from shocked ejecta looks very similar to the fleecy complexes detected in X-rays in both Tycho and SN 1006. The earliest time shown in figure 8 (top right) is just after the end of the instability saturation period mentioned in section 3. Ejecta structures at this time in the central region are visible as a filamentary network. In the time between the early image and the end of the simulation (bottom left of the figure) the Rayleigh-Taylor instabilities have grown, sheared, and merged into each other. Figure 9 compares the three different runs at $t = 2.0$ to the SW quadrant of Tycho's SNR to illustrate the effect of compressibility on
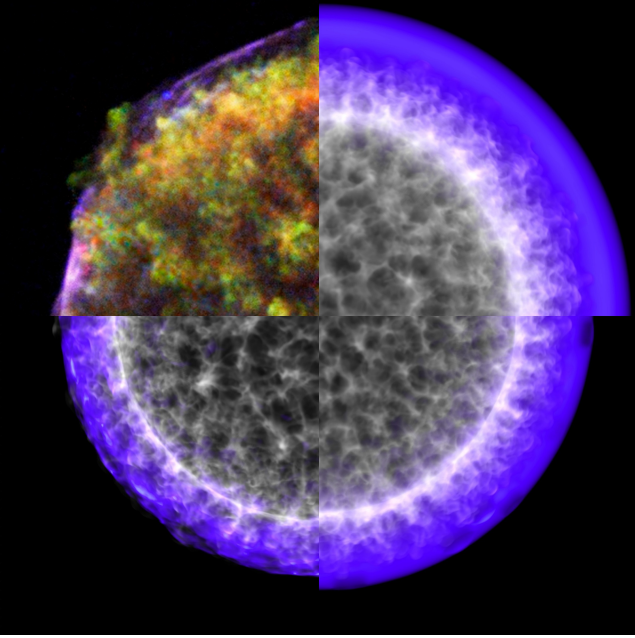
**Figure 9.** Images showing the effect that changing the adiabatic index $\gamma$ of the simulation has on the resultant remnant. The SW quadrant of Tycho's SNR is included at the top left for comparison. Clockwise from the top right: the $\gamma = 5/3$ run, the $\gamma = 4/3$ run, and the $\gamma = 6/5$ run. All three projections are scaled to the correct relative size so interface locations can be directly compared. Image of Tycho taken from Warren et al. (2005).

remnant morphology. The rounded mushroom caps of the Rayleigh-Taylor structures at $\gamma = 5/3$ are still noticeable at $\gamma = 4/3$, though the center of the remnant is darker relative to the limb brightening. By $\gamma = 6/5$ the RT structures' caps are no longer generally round: the greater compressibility has resulted in much longer, thinner fingers of shocked ejecta, and extensive interaction with the forward shock has bent or otherwise warped many of them.

### 4.2    CD shape, relation to FS

Figure 8 compared the $\gamma = 5/3$ remnant at three different times to one quadrant of SN 1006. The structures visible at the center of SN 1006 are smaller in angular size than the RT structures at the center of the $t = 2.0$ image, but also less filamentary than the similarly-located ejecta at $t = 0.12$. The RT fingers in both the $\gamma = 5/3$ and the $\gamma = 4/3$ remnant are largely oriented along radial lines, as seem to be the structures at the edge of SN 1006. Furthermore, the structures at the edge of SN 1006 appear to be more discrete, that is, with a better-defined edge to each structure. The enhanced edges visible in the structures of SN 1006 allow them to stand out against each other, as opposed to the less distinct haze outside the limb brightening in the $t = 0.75$ and $t = 2.0$ images. There is no obvious cutoff in limb brightening to mark a reverse shock in the image of SN 1006, as the contrast is dominated by the large-scale gap in emission in the SE quadrant.

As the compressibility of the fluid increases, interaction with the contact discontinuity can cause bubbles at the forward shock, noticeable in both the $\gamma = 4/3$ and the $\gamma = 6/5$
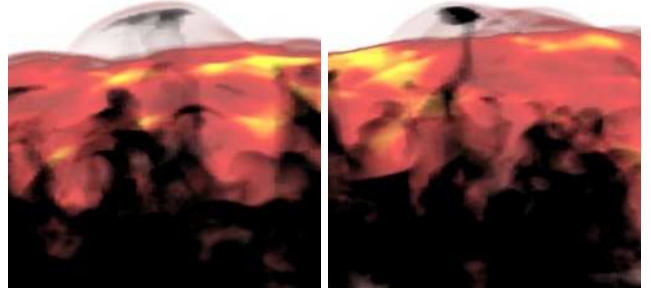


**Figure 10.** Magnified views of two locations from the $\gamma = 6/5$ run where knots of ejecta seem to have overtaken the forward shock.

images in figure 5. However, these bubbles are much fainter at their maximum radial extent than the shocked ISM at their base, so they do not generally show up in projection. One such bubble is visible in the $\gamma = 4/3$ quadrant of figure 9 as a thin bright rim of emission ahead of a darker patch. The situation is more extreme still with the $\gamma = 6/5$ run, where the bubbles comprise a much larger fraction of the forward shock. Instead of the mostly smooth emission of the $\gamma = 5/3$ and $\gamma = 4/3$ runs, the projected forward shock of the $\gamma = 6/5$ run shows up as a chaotic network of projected bubbles, with single bubbles at the edge of the remnant too dim to appear in projection. It is for this run that the approximation to X-ray synchrotron emission (discussed at the start of the section) is most telling; if the emission decayed more quickly, the diffuse shell of emission would resolve into a filamentary network tracing out the locations of the bubbles at the forward shock. Comparison between figures 5 and 9 implies that the locations around the rim of Tycho's SNR where emission from the forward shock is absent could be artifacts of interaction between the shocked ejecta and the forward shock.

One feature captured by the $\gamma = 6/5$ run, not present in the other two, is locations around the edge where knots of ejecta seem to be visible beyond the forward shock. Two examples have been enlarged and recolored for ease of viewing in figure 10. The effect is an illusion caused by the faint bubbles of forward shock emission discussed in the previous paragraph, and by projection effects; the contact discontinuity is always inside the forward shock in the three-dimensional data. Even in the $\gamma = 6/5$ run, such protrusions are rare, occurring only a few times around the rim of the remnant; they are absent entirely from the $\gamma = 4/3$ and $\gamma = 5/3$ runs. With the smooth ejecta used in our runs, the ISM must be highly compressible before the forward shock is close enough to the contact discontinuity to be significantly affected by RT fingers. An alternative explanation was suggested by Orlando et al. (2012), who conclude that the separation between the CD and FS is an indication of ejecta structure rather than of cosmic ray acceleration: overdensities in the ejecta drive instability growth, resulting in more interaction at higher compressibilities than seen in our simulations.

The knots pictured in figure 10 are roughly the same angular size, $\lesssim 10°$, as the protrusions around the rim of
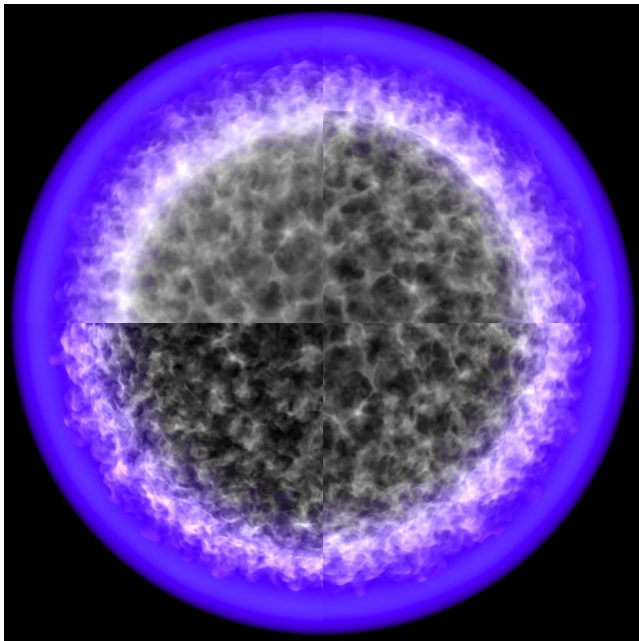
**Figure 11.** Above, images of one simulated remnant with increasingly high cutoffs. *Top left*: an image with no cutoff in place; *top right*: $\tau_{\min} = 0.8$; *bottom right*: $\tau_{\min} = 1.6$; *bottom left*: $\tau_{\min} = 2.4$. Using the scale factor from equation 7 and setting all parameters to unity, the three cutoffs correspond in physical units to $\tau_{\min} = 2.52 \times 10^9 \, \mathrm{cm}^{-3} \, \mathrm{s}$, $\tau_{\min} = 5.04 \times 10^9 \, \mathrm{cm}^{-3} \, \mathrm{s}$, and $\tau_{\min} = 7.56 \times 10^9 \, \mathrm{cm}^{-3} \, \mathrm{s}$ respectively. All images are at $t = 2.0$ for the $\gamma = 5/3$ run.

SN 1006 (in the SE, S, and SW) and Tycho (in the S and W). We conclude that these features can be generated by fluid instabilities alone, without any inhomogeneities present within the unshocked ejecta or the unshocked ISM. There are no features in the $\gamma = 6/5$ run on the same scale as the shelf of thermal emission at the N rim of Tycho or the tiered structure in the NE polar cap of SN 1006, both of which are many tens of degrees across. The inability of the Rayleigh-Taylor instability to produce these features points at inhomogeneities in the ejecta, the magnetic field strength around the progenitor, or the ISM.

### 4.3 Ionization age cutoffs, limb brightening, and angular variation

Assuming that X-ray thermal emissivity is proportional to $n^2$ in visualizing data potentially overestimates emission from the remnant: not all matter is radiating in all wavelengths at all times, due at least in part to deviations from ionization equilibrium. To account for this effect in the three-dimensional simulations, ionization age cutoffs were implemented during visualization, below which shocked ejecta were assumed to be X-ray faint. The effect on observed morphology is shown in figure 11, which (clockwise from the top left) sets the cutoff for emission at successively higher levels for the $\gamma = 5/3$ run at $t = 2.0$. There is no cutoff for the top left quadrant ($\tau_{\min} = 0.0$), and by the bottom left a high cutoff ($\tau_{\min} = 2.4$) has eliminated about half of the shocked ejecta by volume. Since recently shocked ejecta is (for the $\gamma = 5/3$ run) well within the innermost extent of
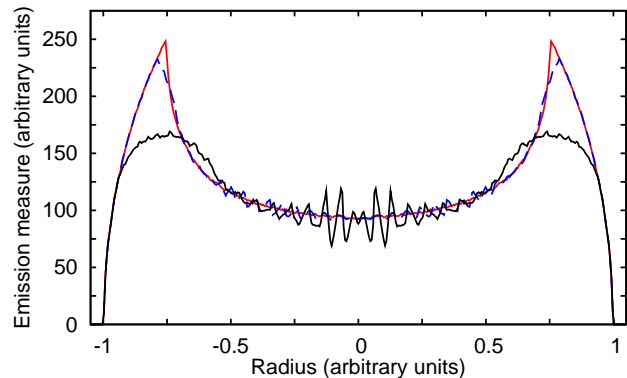


**Figure 12.** Illustration of the effect of a disrupted inner edge on the emission from a hollow shell. The solid red line shows a projection through a 2-D hollow shell; the radius of the inner edge is 0.75 times that of the outer edge. The dashed blue line is a projection through the same shell, but with the inner surface perturbed as $1 + 0.05 \sin(40\theta)$. The solid black line is similar, but with the perturbation given by $1 + 0.25 \sin(40\theta)$. Towards the center of the image the perturbations are nearly parallel to the line of projection, accounting for the noise visible in the two perturbed cases.

the contact discontinuity, the cutoff preferentially eliminates smooth shells of recently shocked ejecta at low $\tau$ and leads to raggedness at the inner edge of emission.

This disruption of the inner boundary to emission primarily alters the strength of the limb brightening effect. This outcome is illustrated in figure 12, in which we generated two dimensional uniform hollow shells, perturbed the interior edge, then projected them from two dimensions to one. Without any perturbations in place, the inner edge is clearly identifiable as the sharp peak in limb brightening; in projections from three dimensions to two, a pronounced drop in brightness would occur. With a regular perturbation of amplitude 5% to the inner radius, the peak of emission no longer exactly traces the unperturbed reverse shock, even though the average radius is unchanged. Instead, the peak is outside that of the unperturbed case, and while the peak of emission is still plain the decay towards the center is no longer as pronounced. When perturbations are 25% of the average radius (an extreme case that isn't suggested by the three-dimensional data), the maximum of emission is now around that of the unperturbed case, but it is no longer a clear peak. Both the interior and exterior regions to the radius of maximum emission show gentle slopes, and the maximum itself is only $\sim 150\%$ of the emission from near the axis of symmetry of the shell.

There is definite limb brightening occuring in Tycho's SNR, but the inner edge to the emission is indistinct. This effect is reproduced successfully by the lower two quadrants in figure 11, although the upper two quadrants (with no cutoff or a low one) still display the reverse shock as a localized drop in emission. Comparison to SN 1006 is less favorable; the limb brightening effect is either across too thin a region (i.e. the northwest quadrant) or too broad a region (the southeast quadrant).

## 5  DISCUSSION

This section elaborates on three topics that have been mentioned only in passing so far. We examine the location of the interfaces (reverse shock, contact discontinuity, and forward shock) in the projected images of figures 8 and 9. We then combine available information throughout the paper with observed quantities to estimate the dynamical age of both SN 1006 and Tycho's SNR. Lastly, we discuss projection effects and associated error with an eye toward future observations of remnants.

### 5.1  Interface locations

Addressing whether our remnants generate the radial structure of Tycho's SNR and SN 1006 requires an analysis of our remnants mimicking the method of Warren et al. (2005) for locating interfaces. With only one "component" representing ejecta instead of nearly a dozen, however, we cannot replicate their procedure exactly. We first divided the remnant into 1440 angular wedges $0.25°$ in width, and created a radial grid with 240 points along each angular wedge. Matching our remnant's radius to the $251''$ of Tycho's SNR, our radial resolution is roughly $1''$. This is finer than the value of $3''$ used in Warren et al. (2005), but the resolution of our data is sufficient to allow it: $\Delta r/r = 1.2 \times 10^{-3}$, so the angular size of a single zone at the edge of the projection is just $0.3''$.

With the projection partitioned into a grid, we located the contact discontinuity, forward shock, and reverse shock at each angular location. We identified the contact discontinuity with the outermost radius where emission from shocked ejecta occurred. This method does not track the true contact discontinuity (shown in figures 1 and 5): as discussed in Appendix A, it biased toward protrusions at greater radius than the average value across the remnant. It is nonetheless very similar to the identification process used to find the CD in Warren et al. (2005) and Cassam-Chenaï et al. (2008). The forward shock was defined as the outermost radius at which intensity reached half the maximum value for each radial spoke. This misses some of the filamentary structures that appear at lower values of $\gamma$, but does approximate the method of Warren et al. (2005).

The reverse shock was found by treating the shocked ejecta as a hollow shell and identifying the maximum value along each radial line. This correctly identifies the location of the reverse shock for every combination of $\gamma$ and $t$ except $\gamma = 5/3$, $t = 2.0$. In that instance, the density gradient in the shocked ejecta causes stronger emission near the contact discontinuity than near the reverse shock. This is visible in the upper left quadrant of figure 11 as a bright ring inside the edge of ejecta emission. The inner edge of emission becomes increasingly ragged or diffuse as $\gamma$ decreases or as we exclude freshly-shocked ejecta from emission calculations (see section 4.3 above). Any maximum value less than 50% of the overall maximum value was deemed to be unresolvable against the background of Rayleigh-Taylor fingers. Because of the Yin-Yang grid used for the simulations, overlap between the two parts of the grid could generate an artificially high value for projected emission at the two angles where the overlap occurs. To prevent this artifact from affecting
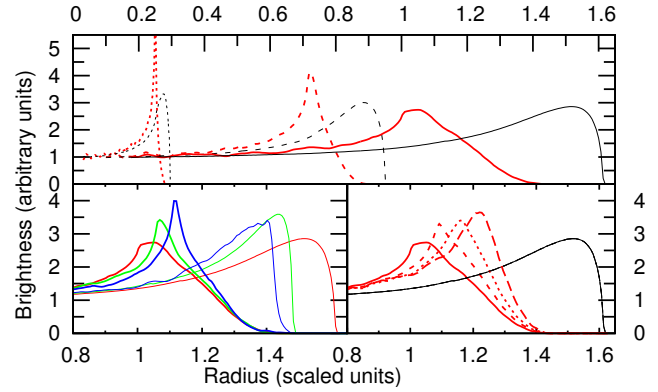


**Figure 13.** Emission intensity as a function of radius for selected line-of-sight projections. All profiles have been scaled to the average brightness of the central region ($R < 0.2R_{FS}$) of that image. *Top*: intensity profiles for the $\gamma = 5/3$ run. Peaking from left to right, $t = 0.12$ (dotted line), $t = 0.75$ (dashed line), and $t = 2.0$ (solid line). The thin black lines trace out intensity due to shocked ISM. *Bottom left*: intensity profiles for the three runs at $t = 2.0$. Peaking from left to right, $\gamma = 5/3$ (red line), $\gamma = 4/3$ (green line), $\gamma = 6/5$ (blue line). The thin lines trace out emissivity of shocked ISM. *Bottom right*: intensity profiles for the $\gamma = 5/3$ run at $t = 2.0$, with ionization age cutoffs in place. Peaking from left to right, $\tau_{min} = 0.0$ (thick solid line), $\tau_{min} = 0.8$ (dotted line), $\tau_{min} = 1.6$ (thin solid line), $\tau_{min} = 2.4$ (dashed line). The thin black line is intensity of shocked ISM.

the 50% threshhold of the reverse shock, the single highest value over all 1440 angular wedges was excluded.

The angle-averaged brightness profiles for selected data sets are shown in figure 13, illustrating the effects of time, compressibility, and an ionization age cutoff on emission. The effects of the ejecta gradient mentioned previously are visible as the plateau in the late-time curve in the top panel.

The radii for the three fluid discontinuities, averaged around the rim of each projection, are gathered in table 3, based off of the preceding analysis of the line-of-sight projections. In this table and for the rest of the paper, we use the notation of Cassam-Chenaï et al. (2008), in which $\hat{R}_{CD}$ denotes the projected radius of the contact discontinuity and $R_{CD}$ the average location of the discontinuity in three dimensions. Comparing $R_{FS}$ between the runs with $\gamma = 5/3$ and $\gamma = 4/3$, it is clear that increasing the compressibility of the fluid has a significant effect on the overall size of the remnant at similar dynamical times, just as with the one-dimensional runs presented in figure 2. The forward shock decelerates less than the reverse shock and the contact discontinuity as the remnant evolves, and all ratios in Table 3 drop with time. Lowering the adiabatic index has the opposite effect, bringing the interfaces closer together and raising the ratios in table 3.

From shock positions alone it may be difficult to distinguish between a younger remnant with less efficient cosmic ray acceleration and a more evolved remnant with more efficient particle acceleration. At roughly the age of Tycho's remnant, the ratio $\hat{R}_{CD}/\hat{R}_{FS}$ for the $\gamma = 5/3$ run is lower than observed in Tycho, as is $\hat{R}_{RS}/\hat{R}_{FS}$. With the $\gamma = 4/3$ simulation, $\hat{R}_{CD}/\hat{R}_{FS}$ is close to that observed in Tycho, but the reverse shock is too close to the forward shock. If the forward shock were more efficient at cosmic ray acceleration than the reverse shock, the effective adiabatic index

**Table 3.** Interface radii and ratios, from 2-D projections and 3-D data

| $\gamma$ | $t$ | $\hat{R}_{\rm RS}$ | $\hat{R}_{\rm CD}$ | $\hat{R}_{\rm FS}$ | $\hat{R}_{\rm RS}:\hat{R}_{\rm FS}$ | $\hat{R}_{\rm CD}:\hat{R}_{\rm FS}$ | $R_{\rm RS}$ | $R_{\rm CD}$ | $R_{\rm FS}$ | $R_{\rm RS}:R_{\rm FS}$ | $R_{\rm CD}:R_{\rm FS}$ | $\xi_{\rm RS}$ | $\xi_{\rm CD}$ |
|---|---|---|---|---|---|---|---|---|---|---|---|---|---|
| 5/3 | 0.12 | 0.250 | 0.279 | 0.296 | 0.845 | 0.943 | 0.249 | 0.265 | 0.297 | 0.838 | 0.892 | <1% | 6% |
| " | 0.75 | 0.725 | 0.873 | 0.951 | 0.762 | 0.918 | 0.716 | 0.800 | 0.952 | 0.752 | 0.840 | 1% | 9% |
| " | 2.0 | 1.009 | 1.391 | 1.616 | 0.624 | 0.861 | 1.005 | 1.229 | 1.615 | 0.622 | 0.761 | <1% | 13% |
| 4/3 | 0.19 | 0.334 | 0.371 | 0.377 | 0.886 | 0.984 | 0.333 | 0.351 | 0.377 | 0.883 | 0.931 | <1% | 6% |
| " | 0.75 | 0.737 | 0.863 | 0.888 | 0.830 | 0.972 | 0.734 | 0.795 | 0.887 | 0.828 | 0.896 | <1% | 8% |
| " | 2.0 | 1.074 | 1.378 | 1.484 | 0.724 | 0.929 | 1.060 | 1.228 | 1.484 | 0.714 | 0.827 | 1% | 12% |
| 6/5 | 0.16 | 0.297 | 0.332 | 0.332 | 0.895 | 1.000 | 0.297 | 0.313 | 0.331 | 0.897 | 0.946 | <1% | 6% |
| " | 0.75 | 0.733 | 0.877 | 0.883 | 0.830 | 0.993 | 0.737 | 0.795 | 0.872 | 0.845 | 0.912 | -2% | 9% |
| " | 2.0 | 1.115 | 1.393 | 1.449 | 0.769 | 0.961 | 1.112 | 1.224 | 1.438 | 0.773 | 0.851 | -1% | 13% |

of shocked ejecta and shocked ISM would differ, leading to varying compressibilities ahead of and behind the contact discontinuity. Previous work offers support for such a situation. Decourchelle, Ellison & Ballet (2000) provided evidence that low magnetic fields lead to negligible acceleration of cosmic rays. In the absence of magnetic field amplification by the reverse shock, the frozen-in magnetic field of the ejecta should be attentuated by expansion, and therefore $\gamma_{\rm eff}$ should be approximately 5/3. Ellison, Decourchelle & Ballet (2005) elaborated on the bijective relationship between magnetic field amplification and DSA, and while studies have been done of magnetic field amplification at Tycho's forward shock (Völk, Berezhko & Ksenofontov 2005), we are unaware of observations suggesting magnetic field amplification at Tycho's reverse shock; Hughes, Rakowski & Decourchelle (2000) did, however, find evidence of efficient cosmic ray acceleration at the reverse shock of 1E 0102.2-7219. Our conclusion echoes that of Warren et al. (2005), which found little evidence for particle acceleration at the reverse shock of Tycho by comparing 1-D hydrodynamic models to the discontinuity radii deteremined in that paper.

## 5.2 Implications for Tycho and SN 1006

The evolution of the exponential model is governed entirely by the scaled age $t$, so attempts to compare the model to observations must determine the dynamical age of the remnant in question. In the previous sections we have examined the effect of scaled time and adiabatic index on the appearance and structure of our simulated remnants, including interface locations, power spectra, and deceleration parameters. Now we will combine these results with observed quantities to estimate the dynamical ages of Tycho and SN 1006, and to discuss the efficiency of cosmic ray acceleration in both remnants. We consider the fleecy ejecta structures in the SNRs, dynamical quantities of the ejecta, and the average radial locations of the fluid discontinuities in determining the age of the two SNRs. We also use deceleration parameters in order to constrain the effective adiabatic index at the forward shock.

Tycho's SNR was first observed in 1572, giving it (at time of writing) a real age of 439 years. This corresponds to a scaled age of $t = 439 \, \mathrm{yr}/T' \approx 1.77 \, (M_e/M_{\rm Ch})^{-5/6} E_{51}^{1/2} n_0^{1/3}$. SN 1006, with a real age of 1005 years, has a scaled age of $t = 4.05 \, (M_e/M_{\rm Ch})^{-5/6} E_{51}^{1/2} n_0^{1/3}$. Despite the difference in age, our simulations strongly suggest that Tycho be dynamically older than SN 1006. The fleecy structures present

in Tycho are, on average, larger in angular size than those observed in SN 1006. In our simulated remnants and their projections, the angular size of the fleecy ejecta structures is almost completely determined by the dynamical age of the remnant (see figures 1, 3, and 8); the size of the structures depends only weakly, if at all, on the compressibility of the fluid (figures 5 and 6).

One way to approach the dynamical age of the remnant is consideration of the motion of the ejecta. Three quantities are relevant here: (i) the free expansion velocity of unshocked ejecta just ahead of the reverse shock, (ii) the bulk radial motion of shocked ejecta near the reverse shock, and (iii) the bulk motion of the ejecta at the contact discontinuity.

(i) The expansion velocity at the reverse shock of SN 1006 is $7026 \pm 13$ km s$^{-1}$ ($v = 0.83 \, (M_e/M_{\rm Ch})^{1/2} E_{51}^{-1/2}$) based on Doppler-shifted absorption lines through the remnant (Hamilton et al. 2007) (the shape of the lines points to asymmetry in the remnant, however, so it is uncertain if this velocity is representative of the reverse shock everywhere). The shock is unlikely to be accelerating cosmic rays efficiently, for reasons outlined in the previous subsection; the effective adiabatic index should therefore be close to $\gamma = 5/3$. In this case, the location of the reverse shock is consistent in one dimension and in three. From 1-D runs, then, we find that a free expansion velocity of 0.83 at the reverse shock corresponds to a dynamical age of $t = 1.0$ for SN 1006 for canonical values of $E_{51} = 1$ and $M_e = M_{\rm Ch}$.

(ii) No observations like those of Hamilton et al. (2007) have been reported for Tycho, but Hayato et al. (2010) fitted pairs of red- and blue-shifted absorption lines to the Fe K$\alpha$ spectral feature of Tycho, and measured the radial velocity by quantifying the relative shift between the center of the remnant and the edge. They report expansion velocities of $4000 \pm 300$ km s$^{-1}$ ($v = 0.47 \, (M_e/M_{\rm Ch})^{1/2} E_{51}^{-1/2}$) for Fe K$\alpha$, which should be associated with freshly shocked ejecta at the reverse shock. The velocity of recently shocked ejecta in our $\gamma = 5/3$ simulation at $t = 0.75$ ($t = 2.0$) is $v = 0.58$ ($v = 0.21$). Interpolation between the two suggests a dynamical age of 1.1 for Tycho.

(iii) Using a similar process for the Si He$\beta$ feature, Hayato et al. (2010) found the expansion velocity to be $4700 \pm 100$ km s$^{-1}$ ($v = 0.56 \, (M_e/M_{\rm Ch})^{1/2} E_{51}^{-1/2}$) for silicon, which they associate with the contact discontinuity. In 1-D the radial velocity of the contact discontinuity is 0.56 at $t = 0.72$. However, in multiple dimensions fluid instabilities cause a range of velocities and densities in the mixing region. The greatest emissivities should occur in the forward tips

**Table 4.** SNR 1006 parameters, assuming $M_e/M_{\mathrm{Ch}} = 1$

| $M_e/M_{\mathrm{Ch}}$ | $E_{51}$ | $v_{\mathrm{RS}}^{(1)}$ | $t^{(2)}$ | $n_0$ (cm$^{-3}$)$^{(3)}$ | $r'_{\mathrm{FS}}$ (pc)$^{(4)}$ |
|---|---|---|---|---|---|
| 1.0 | 1.0 | 0.83 | 0.98 | 0.014 | 8.84 |
| 1.0 | 1.5 | 0.68 | 1.35 | 0.020 | 9.31 |
| 1.0 | 3.0 | 0.48 | 2.15 | 0.029 | 10.42 |
| 1.0 | 4.0 | 0.42 | 2.50 | 0.030 | 11.03 |
| 1.0 | 6.0 | 0.34 | 3.18 | 0.031 | 12.04 |
| 1.0 | 9.0 | 0.28 | 3.67 | 0.028 | 13.37 |
| 1.5 | 2.0 | 0.72 | 1.25 | 0.029 | 9.13 |
| 1.5 | 2.5 | 0.64 | 1.48 | 0.035 | 9.39 |
| 1.5 | 3.0 | 0.59 | 1.66 | 0.037 | 9.69 |
| 1.5 | 4.0 | 0.51 | 2.00 | 0.042 | 10.17 |
| 1.5 | 6.0 | 0.42 | 2.50 | 0.043 | 11.03 |
| 1.5 | 9.0 | 0.34 | 3.10 | 0.047 | 11.99 |

(1) 7026 km s$^{-1}$ in scaled units.
(2) Time at which reverse shock velocity equals $v_{RS}$.
(3) Density required for the scaled time $t$ to correspond to 1001 yr.
(4) At scaled time $t$.

of Rayleigh-Taylor structures, which expand more rapidly than the rest of the contact discontinuity. The highest ionization ages should also occur in the R-T structures. In the $\gamma = 5/3$ run, the 10 per cent of the ejecta with the highest ionization age has a radial velocity of 0.65 at $t = 0.75$; this decreases to $v = 0.26$ by $t = 2.0$. Interpolating between the two numbers, the results of Hayato et al. (2010) applied at the contact discontinuity of our 3-D simulations imply that Tycho's dynamical age is 1.0.

The estimated age around 1.0 for both Tycho and SN 1006 conflicts with the size of the ejecta structures, which should be a marker for relative age. The reason for this difference is not clear.

We now assess the ramifications of observed fluid velocities on the parameters ($n_0$, $M_e$, and $E_{51}$) of the two SNRs. As mentioned in section 2, the scaling factor for time depends inversely on both the explosion energy and the interstellar density (it also depends on the ejecta mass, but we see little reason why this should deviate from $M_{\mathrm{Ch}}$). There is a good deal of evidence that the ISM around Tycho is denser than that around SN 1006: the inferred densities around Tycho from X-ray (Cassam-Chenaï et al. 2007), $\gamma$-ray (Völk, Berezhko & Ksenofontov 2008), and optical observations (Kirshner, Winkler & Chevalier 1987) all support a value for $n_0$ of 0.1-0.3 cm$^{-3}$ in the west, with higher densities in the east. Assuming $E_{51} = 1$, the scaled and physical ages of Tycho match if $n_0 = 0.18$ cm$^{-3}$, consistent with observations.

Around SN 1006, observations suggest a lower interstellar density. Acero, Ballet & Decourchelle (2007) found the X-ray emission measure of the forward shock and calculated an ISM density of 0.05 cm$^{-3}$ in the southeast quadrant, and argued that the density was roughly constant everywhere except the filamentary northwest rim. Using expansion data, Katsuda et al. (2009) determined the density at the northeast to be 0.085 cm$^{-3}$. A very low ISM density, $n_0 = 0.014$ cm$^{-3}$ if $E_{51} = 1$, is required to match the dynamical and physical ages (see table 4). This is lower than either observational estimate, though it is within model-dependent uncertainties of the value presented by Acero,

Ballet & Decourchelle (2007). Also visible in table 4 is that the physical age of SN 1006 cannot be matched to the velocity measurements of Hamilton et al. (2007) for any ambient density greater than about 0.030 cm$^{-3}$, which itself requires $t > 2.15$ and $E_{51} > 3.0$. We can impose an additional constraint on the parameters of SN 1006 by considering its size: at a distance of $2.18 \pm 0.08$ kpc (Winkler, Gupta & Long 2003), and with an average radius of 14.5$'$ in the SE quadrant (Cassam-Chenaï et al. 2008), the radius of the forward shock is 9.19 parsecs. Under the assumption that $M_e/M_{\mathrm{Ch}} = 1$, the explosion energy $E_{51} = 1.4$ and ISM density $n_0 = 0.019$ are consistent with SN 1006's age, reverse shock velocity, and size. These parameters suggest a scaled age of 1.3 for SN 1006. If we relax the assumption that $M_e = M_{\mathrm{Ch}}$, we again find a consistent solution. Table 4 shows the same calculations if $M_e/M_{\mathrm{Ch}} = 1.5$. It can be seen that the upper limit on $n_0$ is 0.047 cm$^{-3}$ in this case. The parameters that match the age, size, and reverse shock velocity are $E_{51} = 2.1$ and $n_0 = 0.030$ cm$^{-3}$; they also imply that SN 1006's dynamical age is 1.3. Such a massive and energetic supernova could be consistent with a white dwarf merger origin for SN 1006.

The deceleration parameter, like the separation between fluid discontinuities and the free expansion velocity of ejecta, is a monotonic function of time. As evidenced by figure 7, it is also sensitive to the effective adiabatic index: for any particular time, decreasing the adiabatic index also lowers the deceleration parameter. Tycho's deceleration parameter is higher along the NW-SW rim (where the remnant is close to spherical symmetry), $0.59 \pm 0.12$ (Katsuda et al. 2010), than is SN 1006's at the NE rim (the only quadrant where such a study has been performed in X-rays), $0.54 \pm 0.06$ (Katsuda et al. 2009), although the two numbers are separated by a single standard deviation. Since the deceleration parameter should decay from 1.0 to 0.4 as a remnant transitions from free expansion to the Sedov phase, these numbers suggest that Tycho is slightly dynamically younger than SN 1006. The large uncertainties in both values do leave open the possibility that the situation is reversed – that the correct deceleration parameter for Tycho is lower than that for SN 1006 – but the data presented in figure 7 offer another interpretation consistent with observations. We posit that, if SN 1006 is dynamically younger than Tycho – or even the same dynamical age – it must be more efficiently accelerating cosmic rays at its forward shock, lowering both its deceleration parameter and effective adiabatic index below Tycho's.

To quantify the difference in adiabatic index of the two remnants, we turn to the forward shock and its separation from the contact discontinuity. There is substantial evidence that both remnants are efficiently accelerating cosmic rays at their forward shock, so we exclude the $\gamma = 5/3$ run and focus on the $\gamma = 4/3$ and the $\gamma = 6/5$ runs. At $t = 1.0$, $\hat{R}_{\mathrm{CD}} : \hat{R}_{\mathrm{FS}}$ is 0.96 and 0.99, respectively, for $\gamma = 4/3$ and $\gamma = 6/5$. This ratio for SN 1006 is 0.98 in the NE polar cap (Cassam-Chenaï et al. 2008). The effective adiabatic index in SN 1006 should therefore be just over 1.2 – at the very least, much closer to $\gamma = 6/5$ than to $\gamma = 4/3$. The estimated adiabatic index is less than 6/5 if the age estimate is increased to 1.3, as suggested by Table 4. In the case of Tycho, $\hat{R}_{\mathrm{CD}} : \hat{R}_{\mathrm{FS}}$ along the western rim (where the remnant appears mostly spherical) is around 0.95. We expect an effective adiabatic index of just over 4/3 for Tycho (this

number increases if the dynamical age decreases, and vice versa). We note that these numbers agree broadly with the results of Kosenko, Blinnikov & Vink (2011), who used 1-D simulations to calculate a range of allowable compressibilities that could match the radial morphology of Tycho and SN 1006, and found that the upper end of SN 1006's range was higher than the upper end of Tycho's.

As mentioned in section 3.1 and table 3, the reverse shock and contact discontinuity are constantly receding relative to the forward shock; the separation between the interfaces could therefore serve as a probe of dynamical age. No reverse shock has been directly observed in SN 1006, but Warren et al. (2005) identified Fe K$\alpha$ emission with the reverse shock in Tycho. Since the location of the contact discontinuity is far less dependent on the adiabatic index than are the locations of the forward and reverse shocks, $\hat{R}_{\rm RS} : \hat{R}_{\rm CD}$ requires fewer assumptions as an indicator of Tycho's dynamical age than does the more commonly quoted figure of $\hat{R}_{\rm RS} : \hat{R}_{\rm FS}$. For Tycho, this value is $0.73/0.96 = 0.76$ (Warren et al. 2005). The same ratio for the $\gamma = 5/3$ run at $t = 0.75$ is 0.83, and has dropped to 0.73 by $t = 2.0$. Interpolation between the two yields a dynamical age for Tycho of 1.6. The ratio $\hat{R}_{\rm RS} : \hat{R}_{\rm FS}$ can be used to estimate Tycho's dynamical age, but requires an assumption about the compressibility of the ejecta and ISM. Using $\gamma = 5/3$ for the ejecta (and $\hat{R}_{\rm RS}$) and $\gamma = 4/3$ for the ISM (and $\hat{R}_{\rm FS}$), the appropriate ratio is 0.82 at $t = 0.75$ and 0.68 at $t = 2.0$. The ratio in Tycho is 0.73 (Warren et al. 2005), which occurs at $t = 1.6$. This result does not change significantly if more compressible ISM is assumed. Intriguingly, velocity measurements and radial morphology each give a consistent estimate for the age of Tycho's remnant, but the two estimates do not agree with each other.

Taken together, the results discussed in this section paint the following scenario for the relative dynamical ages and effective adiabatic indices of the remnants of Tycho's SN and SN 1006. The size of ejecta stuctures and Tycho's radial morphology suggests that it is the older remnant, but available velocity information implies that both remnants have roughly equal dynamical ages. In either case, SN 1006 is more efficiently accelerating cosmic rays at its forward shock. We calculate a dynamical age for SN 1006 of 1.3 based on the free expansion velocity of unshocked ejecta and on the known size of the remnant. At this age, the separation between the forward shock and the contact discontinuity implies an effective adiabatic index of 6/5. If the scaled age of Tycho's SNR is 1.0 as suggested by expansion velocity of its ejecta, we find that $\gamma_{\rm eff} \approx 4/3$ at its forward shock. Given the simplicity of our model, the disparate age estimates in the case of Tycho, and the numerous factors affecting the remnants' actual expansions, however, further study is warranted before firm conclusions can be drawn.

## 6 CONCLUSIONS

We have performed high resolution three-dimensional simulations of a Type Ia supernova remnant using an exponential ejecta profile and assuming homogenous ejecta and ISM. The Rayleigh-Taylor instability is clearly capable of generating the fleecy structures observed in Tycho's SNR. Comparison against SN 1006 is qualitatively less favorable

due to the orientation and spacing of the structures in that remnant. The ejecta and ISM in all simulations were smooth at initialization, implying that clumpiness is not a necessary condition to generate the structures observed in Tycho. This result depends critically on evolving the simulations long enough time for the instabilities to saturate, independently of the compressibility of the fluid. While our simulations reproduced the central regions of both remnants well, they require a relatively high cutoff in ionization age to capture the indistinct limb brightening seen in Tycho, and qualitatively fail to match SN 1006.

After consideration of several observables tied to dynamical age – such as expansion rate of ejecta at the reverse shock, average radii of fluid discontinuities, and deceleration parameter for select regions around the rim – we find that observed parameters are inconsistent in the case of Tycho's SNR, with radial structure and ejecta morphology presenting a different age ($t = 1.6$) than observed ejecta velocities ($t = 1.0$). Taking the lower value as the more accurate, Tycho's effective adiabatic index is slightly higher than 4/3 at its forward shock. SN 1006's dynamical age is approximately 1.3, and accurate measurements of its distance and size allow us to calculate $E_{51} = 1.4$ and $n_0 = 0.019$ cm$^{-3}$. Acceleration of cosmic rays at the forward shock of SN 1006 is more efficient than at that of Tycho's SNR: $\gamma_{\rm eff}$ is 6/5.

Although shape of the contact discontinuity depends on adiabatic index and compressibility of the ejecta, its average radius does not for the period of time covered by our simulations. Further, the shape of the CD, especially given the close proximity to the forward and reverse shocks at low $\gamma$, affects the shape of the shock fronts. For the lowest value of $\gamma$ used, knots of ejecta appear to protrude outside the forward shock, but in reality lie just inside faint bubbles of emission from shocked ISM. This does not happen on angular scales as large as the shelf of emission in NE Tycho or the polar region of emission in NE SN 1006. Since instabilities and smooth ejecta cannot generate those features, something else (inhomogeneity in ISM, ambient magnetic fields, or asymmetric explosion) must be necessary. Studies including inhomogenous ejecta or an ambient magnetic field to azimuthally affect cosmic ray production offer additional insight into the large-scale structure of both of these remnants.

## REFERENCES

Acero F., Ballet J., Decourchelle A. 2007, A&A, 475, 883.
Baade W. 1945, ApJ, 102, 309.

Baldwin J. E. Edge D. O. 1957, The Observatory, 77, 139.

Blondin J. M., Borkowski K. J., Reynold S. P. 2001, ApJ, 557, 782.

Blondin J. M., Ellison D. C. 2001, ApJ, 560, 244.

Blondin J. M., Lundqvist P., Chevalier R. A. 1996, ApJ, 472.

Cassam-Chenaï G., Hughes J. P., Ballet J., Decourchelle A. 2007, ApJ, 665, 315.

Cassam-Chenaï G., Hughes J. P., Reynoso E. M., Badenes C., Moffet D. 2008, ApJ, 680, 1180.

Chevalier R. A., Blondin J. M., Emmering R. T. 1992, ApJ, 392, 118.

Colella P., Woodward P. R. 1984, J. Comp. Phys., 54, 174.

Decourchelle A., Ellison D. C., Ballet J. 2000, ApJ, 543, 57.

Dickel J. R., Eilek J. A., Jones E. M., Reynolds S. P. 1989, ApJs, 70, 497.

Dickel J. R., van Breugel W. J. M., Strom R. G. 1991, ApJ, 101, 2151.

Dobler W., Haugen N. E., Yousef T. A., Brandenberg A. 2003, Phys. Rev. E, 68, 026304.

Dwarkadas V. V. 2000, ApJ, 541, 418.

Dwarkadas V. V., Chevalier R. A. 1998, ApJ, 497, 807.

Ellison D. C., Decourchelle A., Ballet J. 2005, A&A, 429, 569.

Ferrand G., Decourchelle A., Ballet J., Teyssier R., Fraschetti F. 2010, A&A, 509, L10.

Fryxell B., Müller E., Arnett D. 1991, ApJ, 367, 619.

Gardner F. F., Milne D. K. 1965, AJ, 70, 754.

Green D. A. 2009, Bull.Astron.Soc.India, 37, 45A.

Gull S. F. 1973, MNRAS, 161, 47.

Hachisu I., Matsuda T., Nomoto K., Shigeyama T. 1990, ApJL, 358, L57.

Hamilton A. J. S., Fesen R. A., Blair W. P. 2007, MNRAS, 381, 771.

Hamilton A. J. S., Sarazin C. L., Szymkowiak A. E. 1986, ApJ, 300, 713.

Hanbury-Brown R., Hazard C. 1952, Nat, 170, 364.

Hayato A. et al. 2010, ApJ, 725, 894.

Hughes J. P., Rakowski C. E., Decourchelle A. 2000, ApJ, 543, 61.

Kageyama A., Sato T. 2004, Geochem. Geophys. Geosyst., 5.

Kane J., Drake R. P., Remington B. A. 1999, ApJ, 511, 335.

Katsuda S., Petre R., Long K. S., Reynolds S. P., Winkler F. P., Mori K., Tsunemi H. 2009, ApJ, 692, L105.

Katsuda S., Petre R., Hughes J. P., Hwang U., Yamaguchi H., Hayato A., Mori K., Tsunemi, H. 2010, ApJ, 709, 1387.

Kirshner R., Winkler P. F., Chevalier R. A. 1987, ApJ, 315L, 135K.

Kosenko D., Blinnikov S. I., Vink J. 2011, A&A, 532, A114.

Krause O., Tanaka M., Usuda T., Hattori T., Goto M., Birkmann S., Nomoto K. 2008, Nat, 456, 617.

McKee C. F., Truelove J. K. 1995, Phys. Rep., 256, 157.

Nomoto K., Thielemann F.-K., Yokoi K. 1984, ApJ, 286, 644.

Orlando S., Bocchino F., Miceli M., Petruk O., Pumo M. L. 2012, ApJ, 749, 156.

Pacholczyk A. G. 1970, Radio Astrophysics. San Francisco: Freeman.

Reynoso E. M., Moffett D. A., Goss W. M., Dubner G. M.,

Dickel J. R., Reynolds S. P., Giacani E. B. 1997, ApJ, 491, 816.

Seward F., Gorenstein P., Tucker W. 1983, ApJ, 266, 287.

Velázquez P. F., Vigh C. D., Reynoso E. M., Gómez D. O., Schneiter E. M. 2006, ApJ, 649, 779.

Vigh C. D., Velázquez P. F., Gómez D. O., Reynoso E. M., Esquivel A., Schneiter E. M. 2011, ApJ, 727.

Völk H. J., Berezhko E. G., Ksenofontov L. T. 2005, A&A, 433, 229.

Völk H. J., Berezhko E. G., Ksenofontov L. T. 2008, A&A, 483, 529.

Wang C., Chevalier R. A. 2001, ApJ, 549, 1119.

Warren, J. S., et al. 2005, ApJ, 634, 376.

Winkler P. F., Gupta G., Long K. S. 2003, ApJ, 585, 324.

Wu C.-C., Leventhal M., Sarazin C. L., Gull T. R. 1983, ApJ, 269, L5.

# APPENDIX A: DIFFERENCES BETWEEN 2-D PROJECTIONS AND 3-D DATA

Projections of an irregular three-dimensional spherical structure are biased towards protrusions from the average radius, so the average radius of the contact discontinuity differs from the observed radius in projection. This bias can be parameterized by a correction factor $\xi_{\mathrm{proj}}$, where $R_{\mathrm{proj}} = (1 + \xi_{\mathrm{proj}})R_{\mathrm{true}}$. The correction factor depends strongly on the degree of structure present in a surface, so the forward and reverse shocks of our model remnants should see minimal correction compared to the contact discontinuity. In Warren et al. (2005) several factors (e.g. the observed power spectrum and expected length of Rayleigh-Taylor fingers) were considered in determining a correction factor of 6% for Tycho, and resulted in a revision from observed ratios (1 : 0.96 : 0.73) to "true" ratios (1 : 0.93 : 0.71). Drawing on the work of Dwarkadas & Chevalier (1998) and Wang & Chevalier (2001), Cassam-Chenaï et al. (2008) arrived at a projection correcting factor of 10% for SN 1006. With access to both projections and fully three-dimensional data, we can directly evaluate the errors of this method.

The projection correcting factor is related to the projected and true discontinuity locations by $(\hat{R}_{\mathrm{CD}}/\hat{R}_{\mathrm{FS}}) = (R_{\mathrm{CD}}/R_{\mathrm{FS}}) \cdot (1 + \xi)$; a similar equation exists for the reverse shock. Table 3, in addition to the interface locations in the projections, also lists both the true discontinuity locations and the projection correction factor for each $\gamma/t$ pair. Both the CD/FS and RS/FS ratios are higher in projection than they are in 3-D for every simulation at almost every time; the two exceptions for $\gamma = 6/5$ are likely caused by the filamentary nature of emission at the forward shock and the extensive interaction between the fluid discontinuities. Additionally, $\xi$ is very nearly 0 for the reverse shocks. This result is in keeping with the relative smoothness of both the forward and reverse shocks as seen in figures 1 and 5. Warren et al. (2005) predicted a $\xi_{\mathrm{proj}}$ of 3% for the reverse shock of Tycho, an overestimation of the structure present in the reverse shock.

For the contact discontinuity, the correction factors range from 6% at the earliest times to 12-13% at the latest, showing remarkable consistency across $\gamma$ despite the changes to the shape of both the forward shock and the contact discontinuity. Cassam-Chenaï et al. (2008) suggested that a $\xi$

upwards of 10% would be necessary to match observations of SN 1006 ($R_{\mathrm{CD}}/R_{\mathrm{FS}} = 0.96$ for the SE quadrant where minimal nonthermal emission is seen) with their one-dimensional simulations. Their runs were carried out to a scaled time of $t \approx 1.2$, depending inversely on the interstellar density in the environment of SN 1006. Given the lack of synchrotron emission observed over this region, for our hydrodynamic models to match that shock ratio we would require an exceptionally low ambient density in those regions (reducing the dynamic age of the remnant) in conjunction with efficient acceleration.